

# Measuring violations of General Relativity from single gravitational wave detection by non-spinning binary systems: higher-order asymptotic analysis

Rhondale Tso<sup>1,2,3, a</sup> and Michele Zanolin<sup>3, b</sup>

<sup>1</sup>*LIGO Laboratory, California Institute of Technology, Pasadena, CA 91125, USA*

<sup>2</sup>*Columbia Astrophysics Laboratory, Columbia University, New York, NY 10027, USA*

<sup>3</sup>*Physics Department, Embry-Riddle Aeronautical University, Prescott, AZ 86301, USA*

(Dated: September 9, 2015)

A frequentist asymptotic expansion method for error estimation is employed for a network of gravitational wave detectors to assess the capability of gravitational wave observations, with Adv. LIGO and Adv. Virgo, to distinguish between the post-Einsteinian (ppE) description of coalescing binary systems and that of GR. When such errors are smaller than the parameter value, there is possibility to detect these violations from GR. A parameter space with inclusion of dominant dephasing ppE parameters is used for a study of first- and second-order (co)variance expansions, focusing on the inspiral stage of a nonspinning binary system of zero eccentricity detectible through Adv. LIGO and Adv. Virgo. Our procedure is more reliable than frequentist studies based only on Fisher information estimates and complements Bayesian studies. Second-order asymptotics indicate the possibility of constraining deviations from GR in low-SNR ( $\rho \sim 15 - 17$ ) regimes. The errors on  $\beta$  also increase errors of other parameters such as the chirp mass  $\mathcal{M}$  and symmetric mass ratio  $\eta$ . Application is done to existing alternative theories of gravity, which include modified dispersion relation of the waveform, non-spinning models of quadratic modified gravity, and dipole gravitational radiation (i.e., Brans-Dicke type) modifications.

## I. INTRODUCTION

Detector enhancements of the LIGO-Virgo network [1–3] could provide the first detections of gravitational waves (GWs), allowing tests of the consistency of General Relativity (GR) beyond current constraints [4] and determine if GR is congruous with future observations in strongly relativistic regimes [5, 6]. This paper considers the parameterized post-Einsteinian (ppE) framework [6, 7], which produces non-GR GW signals through set parameters. Such a framework can encompass signals from various alternative theories of gravity as a parameterized enhancement to existing GR templates. It is an extension to prior efforts in testing post-Newtonian (PN) coefficients [8–10] through alterations in the dynamics of the orbital motion and emission process for binary systems.

In this paper we quantify the capability of laser interferometers to detect violations of GR, with a single detection of a compact binary coalescence signal, by assessing if the error on the ppE parameters are larger than the separation of modified gravity values with respect to standard GR values. Errors are computed with the most accurate frequentist approach to date by computing the errors as inverse power series in the signal-to-noise ratio (SNR), where the first order is the inverse of the Fisher information matrix [11–13]. Second-order terms of these expansions have been previously used for estimating the errors of physical parameters in compact binary coalescence waveforms and in quantifying the accuracy in the direction of arrival reconstruction for a network of laser

interferometers. The approach adopted here is an improvement with respect to the simple use of inverse Fisher matrices, known to underestimate errors in low-SNR detections. The inverse Fisher matrix diagonal elements, also known as the Cramer Rao lower bound (CRLB), is a lower limit in the error of any unbiased estimator. There is however no guarantee that any estimator is capable to actually attain such a bound for part or the whole range of values the physical parameters can assume. This is the reason why the CRLB often largely underestimate the actual error of parameter estimation procedures.

Bayesian methods were recently applied to test modified GR signals through consistency tests [14, 15], and the ppE framework [16]. Refs. [14, 15] developed a framework to detect a violation without the assumption of a type of model or waveform. Here no parameterized waveform was assumed, thus no need for introducing new parameters, and its results still hold for a family of waveforms as described by the ppE framework. Through Bayesian selection, as described in Ref. [17], the work of Ref. [16] constrained the range of ppE parameter values. While the comparison of the second order calculations in this paper and the frequentist CRLB is well defined, the comparison with the Bayesian studies to detect violations of GR from the same scenario require more care. The Bayesian studies have the goal to describe the variance of the pipelines employed in LIGO, in the presence of priors that are considered safe. As discussed in this paper, in subsections IIIB, IIIC, and IIID, the Bayesian uncertainties are larger than the inverse Fisher matrix estimates. However, in order to give an exact interpretation of the relationship of the Bayesian errors to the second order frequentist corrections of the CRLB presented here, we would need to have quantitative estimates to the impact of the priors (see for example the discussion in

<sup>a</sup> rtso@ligo.caltech.edu

<sup>b</sup> zanolin@ligo.mit.edu

Ref. [18] of the effects of priors) and the optimality of the Bayesian pipelines. In the current draft, we document the relative value of the uncertainties for the scenarios where this is possible, but the caveats above stand. The current study and the Bayesian studies answer slightly different questions, but provide complementary understanding of the non-GR waveform detection problem.

In this study, we continue the exploration of a frequentist approach developed in Refs. [11–13] to have a better understanding of the true lower limit that any estimator could obtain for the case of detecting violations of GR from the single detection of the inspiral of compact binaries. Maximum likelihood estimators in the limit of large SNR attain the CRLB, which is given by the diagonal elements of the inverse of the Fisher information matrix. The inverse of the Fisher matrix only depend on the curvature of the estimator probability distribution around the true value and not from the presence of side lobes or asymmetries (which cause the error to inflate with respect to the CRLB). The benefits of using the second order of the expansions is in the fact that they depend up to the fourth derivative of the likelihood function and, therefore, are sensitive to asymmetries and side lobes of the estimator probability distribution (similar to the change in the accuracy of a Taylor expansion when extended to higher orders). Also, in the past [11–13], the comparison of the second order with the first order provided an analytical understanding of the reasons the CRLB could not be met (for example, in Ref. [12], a novel relationship between the Kurtosis of the probability distribution of the estimator and the SNR was derived to understand when the CRLB could be met).

In addition, this work extends the Fisher information based results of Ref. [8–10], which perform error estimations by modifying PN coefficients. We also extend Fisher-based assessments of specific alternative theories [19–23]. Specifically, this paper considers phase modification in the *restricted* ppE framework [6], considering the ppE framework as a general enhancement to existing `TaylorF2` [24, 25] GR templates in a three detector LIGO-Virgo network [1–3]. Calculations in this limit were chosen since deformations to the GW’s phase are expected to be more resolvable [16, 26] and complements recent Bayesian methods testing deviations from GR [14, 15]. Second-order frequentist constraints produced in this paper are at the same order of magnitude of Bayesian model selection [16], where our errors are quantified at the one sigma level. Errors increase as the parameter space is enlarged and as error estimates of ppE parameters grow, second-order errors of parameters such as the chirp mass, symmetric mass ratio, and time of coalescence also inflate.

The paper is summarized as follows: Section IA introduces the signal model used. Section II presents the parameter space and the expansion model, in particular subsection IIB discusses alternative theories of gravity covered in this paper and the asymptotic MLE expansion model is discussed in subsection IIC. Finally, section III

assesses the results, as applied to a two-dimensional ppE parameter space (III A) and a seven-dimensional parameter space of equal mass (III B) and unequal mass (III C) systems with physical parameters included. Results are applied to existing alternative theories of gravity in III D. A summary and discussion is given in section IV.

## A. Signal Model

The waveforms are assumed to be produced by a non-spinning binary system with all orbital eccentricity information lost when entering the frequency bandwidth of Adv.LIGO and Adv.Virgo. Fourier transform of the signal, through stationary phase [27, 28], acquires the following form,

$$s_{\text{GR}}^I(f) = A_{\text{GR}}^I(f) e^{i(\psi_{\text{GR}}(f) - 2\pi f \tau_I - \Phi_0^I)}, \quad f < f_{\text{merg}} \quad (1.1)$$

for the inspiral stage of the compact binaries. For the phase  $\psi_{\text{GR}}(f)$  and amplitude  $A_{\text{GR}}^I(f)$  the standard `TaylorF2` model [24, 25] is used.

The signal of a collection of alternative theories of gravity is simply the form (1.1) modulated in the phase and amplitude as:

$$\begin{aligned} A_{\text{GR}}^I(f) &\rightarrow A_{\text{GR}}^I(f) (1 + \delta A(f)), \\ \psi_{\text{GR}}(f) &\rightarrow \psi_{\text{GR}}(f) + \delta \psi(f). \end{aligned} \quad (1.2)$$

The additional terms amending the phase and amplitude are a general series of scaling parameters  $\alpha_i, \beta_i \in \mathfrak{R}$  and in some instances arguments call for integer exponentials of  $\nu \eta^{1/5}$  [29, 30], where  $\nu = (\pi M f)^{1/3}$  for total mass  $M$  and  $\eta = m_1 m_2 / M^2$ . Here the analysis is done at leading order in the ppE parameters, i.e.,

$$\begin{aligned} \delta A_{\text{ppE}}(f) &= \alpha (\nu \eta^{1/5})^a, \\ \delta \psi_{\text{ppE}}(f) &= \beta (\nu \eta^{1/5})^b, \end{aligned} \quad (1.3)$$

At each interferometer the signal is assumed to be recorded with additive noise as in Ref. [13]. Frequency dependent noise for Adv.LIGO are interpolated from the official power spectral density [31] of high-power, zero-detuning. Adv.Virgo is assumed to have the sensitivity given in Ref. [32]. For error analysis, and upcoming integrations, the lower cutoff frequency is set to  $f_{\text{low}}$  and the upper cutoff is set to the upper limit for reliability in the inspiral of the waveform template, i.e., the innermost stable circular orbit (ISCO) frequency,

$$f_{\text{low}} = 20 \text{ Hz}, \quad f_{\text{up}} = f_{\text{ISCO}} \approx (6^{3/2} \pi M)^{-1}.$$

Discussion of 1.1 is presented in Appendix A.

The asymptotic maximum likelihood estimate (MLE) approach is first applied to a two-dimensional ppE parameter space (when the physical parameters are known) of equal-mass systems. Only phase corrections are assumed through unknown ppE parameters ( $\beta, b$ ), while  $b$  probes modifications at PN-orders 0.0-3.0 of the

**TaylorF2** model (of a PN-order 3.5 phase). Based on Ref. [11–13] this approach is expected to give overly optimistic errors. Not surprisingly, the Fisher information error estimates presented here for the ppE parameters are at least an order of magnitude smaller than results with Bayesian model selection [16]. Here compact binaries are binary black hole (BBH) systems of a 1:1 mass ratio  $(m_1, m_2) = (10, 10)M_\odot$  and binary neutron star (BNS) systems of masses  $(m_1, m_2) = (1.4, 1.4)M_\odot$ .

Computations are then extended to a seven-dimensional parameter space with the inclusion of physical parameters. In this study,  $\beta$  is varied along  $b = -3, -7$  for a BBH 1:1, 1:2, and BHNS system (1:2 system has masses  $(m_1, m_2) = (5, 10)M_\odot$  and BHNS has masses  $(m_1, m_2) = (1.4, 10)M_\odot$ ). The reason for  $b = -3$  is that it simulates modifications to the dispersion of a GW (e.g., massive gravitons or Lorentz violations [20, 23]). Also,  $b = -7$  simulates weak-field modifications for dipole gravitational radiation (e.g., Brans-Dicke [6, 19]) and the non-spinning, even-parity sector of quadratic modified gravity (e.g., Einstein-Dilation-Gauss-Bonnett, or EDGB, gravity [33, 34]). Distinguishability from GR is denoted as the condition that errors are smaller than the separation between parameters of the GR-limit and that of some alternative theory.

## II. PARAMETER SPACE AND EXPANSION

Thirteen parameters are necessary in the description of the GW: this includes two mass terms, four angles (two source location and two waveform angles), two coalescence parameters, distance to the source, and four ppE parameters in the leading order approximation  $(\alpha, \beta, a, b)$ . In some instances singular Fisher matrices might appear, indicating that the resolvable parameter space is smaller. In these situations the Fisher matrix can still be used to study the errors of a reduced (and resolvable) parameter space.

### A. Parameter space

The distance  $D_L$  is excluded from the error estimates because the amplitude has a dependency on both mass and distance parameters, and the independent treatment of both is unresolvable as already indicated in Ref. [13]. The coalescence phase is also not included because estimations of  $\phi_c$  is relevant only when a full waveform (inspiral, merger, and ringdown) is implemented. The polarization  $\psi$  is excluded because results tend to be independent of it [13]. Derivatives of the fitting factor (2.1) with respect to the binary’s inclination  $\epsilon$  evaluated at, or in a neighborhood of,  $\epsilon = 0$  are roughly zero leading to impossibility to estimate  $\epsilon$  and singular Fisher matrices (thus invertibility is also compromised). Keeping other parameters fixed and varying only  $\epsilon$  produces change in the SNR, with a rescaling of the distance replicating

our low-SNR study. Sky patterns of the errors remain roughly consistent when varying  $\epsilon$ . So  $\epsilon$  is also excluded in this low-SNR analysis. For these reasons the physical parameter space vector is reduced to five parameters labeled as  $\theta_{\text{phys}}^i = \{\eta, \log \mathcal{M}, t_c, \text{lat}, \text{long}\}$ .

Throughout this paper amplitude modulations are to be held fixed to that of GR:  $\alpha = 0$ , because the same effect could be produced by changing physical parameters like distance or mass. Such an approach supposes that GR-violating amplitudes in the waveform are suppressed or modifications manifest only in waveform propagation.<sup>1</sup> Also, recent work suggests that GR modifications produced during the generation of a waveform can be disentangled from that produced during propagation [29], thus, in the event that phase deformation dominates GR-violating effects, amplitude modifications can be disregarded. Calculations in this restricted framework are performed with modifications at various PN-orders in the phase, where in the strong-field regime discrete values of  $b$  controls what PN-order correction is constituted for free parameter  $\beta$  (GR result:  $\beta = 0$ ).

A qualitative way to study the influence of ppE parameters  $(\beta, b)$  on a GR signal can be obtained through the correlation of the signals by means of the fitting factor ( $FF$ ) [26],

$$FF = \max_{\vec{\zeta}} \left( \frac{\langle s_1(\vec{\lambda}) | s_2(\vec{\zeta}) \rangle}{\sqrt{\langle s_1(\vec{\lambda}) | s_1(\vec{\lambda}) \rangle} \sqrt{\langle s_2(\vec{\zeta}) | s_2(\vec{\zeta}) \rangle}} \right) \quad (2.1)$$

Here the  $\langle \cdot | \cdot \rangle$  represent noise weighted inner products [13, 35] and  $s_{1,2}$  are GW signals controlled by general parameter space vectors  $\vec{\lambda}$  and  $\vec{\zeta}$ . Each integration is done from 20 Hz to  $f_{\text{ISCO}}$  with the noise curve of Adv. LIGO [31] “high-power-zero-detuning.” Our exact waveform  $s_1$  is represented by a **TaylorF2** waveform, whereas, a modified-**TaylorF2**, formed through (1.2) and (1.3), acts as  $s_2$ . So  $\vec{\lambda}$  is the GR-limit parameter space vector and  $\vec{\zeta}$  is that of the ppE parameter space. The inner products are maximized over evenly spaced parameters  $\vec{\zeta}$  to provide a  $FF$ -value, where  $FF = 1$  represents an exact match between signals. Both **TaylorF2** models are suppressed to PN-order 2.5 in the phase, a prescription having no effect in this preliminary analysis. In the denominator of (2.1), amplitude parameters normalize to leave  $f^{-7/3}/S_h$  in each integrand. The numerator retains integrand  $(f^{-7/3}/S_h)e^{i\Delta\psi(f; \vec{\lambda}, \vec{\zeta})}$ , where,

$$\Delta\psi(f; \vec{\lambda}, \vec{\zeta}) = \psi(f; \vec{\lambda}) - \psi(f; \vec{\zeta}) - \delta\psi_{\text{ppE}}(f)$$

and, in fixing  $b$  and varying  $\beta$ , the parameters needing to be maximized over are  $\vec{\zeta} = \{t_c, \phi_c, \eta, M_{\text{tot}}\}$ . Millisecond

<sup>1</sup> Modifications to just propagation could surface through alterations in the dispersion of the GW, with alterations stemming from waveform generation excluded [20, 23]. Past studies also indicate modulations are most sensitive to phase modulations [16, 26].

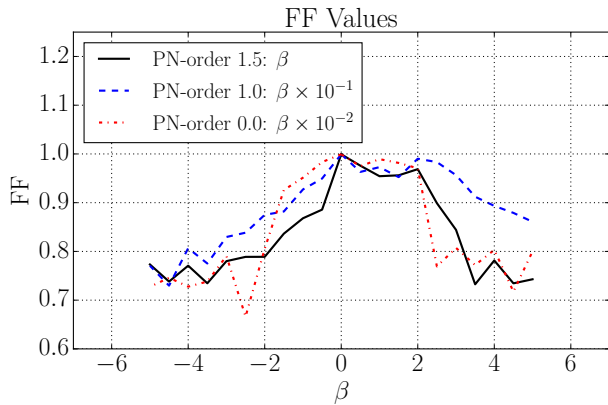


FIG. 1. Fitting factors (2.1) for a range of  $\beta$  with  $b$  fixed to produce PN-order 0.0, 1.0, and 1.5 modifications for a system of:  $m_1 = m_2 = 10M_\odot$  and  $t_a = \phi_a = 0$ . Adv. LIGO noise is assumed. Since the range of  $\beta$ -values scale differently at each PN-order modification, each  $\beta$ -interval is scaled (as labeled in the legend). For example, in the PN-order 0.0 modification the  $\beta$  values in the domain are each scaled by  $10^{-2}$ .

spacing is considered for  $t_c$  and parameters are evenly spaced in intervals:  $0.05 \leq \eta \leq 0.25$ ,  $0.5M_{\text{tot}} \leq M_{\text{tot}} \leq 1.5M_{\text{tot}}$ , and  $-\pi \leq \phi_c \leq \pi$  for maximizing  $FF$ .

Figure 1 displays the results for an equal-mass system of  $m_1 = m_2 = 10M_\odot$  and  $t_a = \phi_a = 0$  for PN-order 0.0, 1.0, and 1.5 modifications in the waveform. Parameters  $\vec{\zeta}$  are maximized over for a variety of  $\beta$ -values. Note that at lower PN-orders the interval of  $\beta$  is scaled differently than the  $-5 \leq \beta \leq 5$  depicted, an interval valid for PN-order 1.5 modifications. The general trend is that the fitting factor is less affected by  $\beta$  for larger PN-order with a skew in the  $FF$ -distribution towards the positive domain of  $\beta$ -values.

## B. Restricted ppE template and existing dephasing alternatives

Variations of  $\beta$  are restricted to fixed PN-order corrections in the phase. For the two-dimensional study  $b$  is fixed to induce modifications at (separately) PN-orders 0.0, 0.5, 1.0, 1.5, 2.0, and 3.0. Higher-dimensional studies specifically target a PN-order 1.0 modification and a weak-field  $b = -7$  modification to address dispersion modification and dipole gravitational radiation. From this reason  $\beta$  is varied with error estimations performed at each  $\beta$ -value. In Ref. [36] an analysis of binary pulsar PSR J0737-3039 [37] placed bounds on ppE parameters (for this binary  $4\eta \approx 1$  as determined from radio pulsar measurements [37]). At PN-order 2.5 ( $b = 0$ ) degeneracies occur with other fiducial parameters, thus is not included. In some theories constraints for  $b = -7$  cannot be implemented from pulsar measurements, due to  $\beta$ 's dependence on mass differences of the system and other theoretical parameters which will be discussed shortly.

With the exception of  $b = -7$ , parameters that venture into weak-field ( $b < -5$ ) are not considered since they are better constrained via binary pulsar measurements [16].

At  $b = -7$ , most existing modifying coefficients depend on parameters that either vanish in the non-spinning model (1.1) or contribute beyond PN-order 3.5. This is the case in specific models of Quadratic modified gravity (QMG), e.g., the odd-parity sector and dynamical Chern-Simons (CS) gravity [34]. As an example, in the circular inspiral of two comparable mass BH's the GR-deviating term of dynamical CS has dependencies on the BH spins  $\hat{S}_{1,2}$  and their relations to their orbital angular momentum  $\hat{L}$ :  $\delta C = \delta C(m_{1,2}, \hat{S}_{1,2}, \hat{L})$  [38]. When the binary system is nonspinning, modifications occur beyond the PN-order 3.5. An exception is the even-parity sector of QMG, like in Einstein-Dilation-Gauss-Bonnet (EDGB) gravity. For even-parity QMG, the violating term depends on the mass differences of the compact objects:  $\beta \propto \zeta_3(1 - 4\eta)$ , a  $b = -7$  correction unresolvable for equal-mass systems [34]. At this same PN-order, examples of dipole gravitational radiation, like Brans-Dicke (BD), can also be assessed. Here BD-like modifications further depend on the difference of parameters which measure the body's inertial mass variations with respect to the local background value of the effective gravitational constant. These so-called ‘‘sensitivity’’ parameters  $s_{\text{BH,NS}}$  are generally set to 0.5 for black holes, so their difference vanish for a BBH system. Only a BHNS system would allow constraints of BD-like modifications since  $0.2 \leq s_{\text{NS}} \leq 0.3$  [39–42].

Beyond modifications during waveform generation, two propagating effects are massive graviton (MG) and simplified versions of Lorentz-violating (LV) theories [20, 23]. Terms to constrain are the graviton Compton wavelength  $\lambda_g$  and parameter  $\lambda_{\text{LV}} = 2\pi\mathbb{A}^{1/(\gamma-2)}$ . Here  $\mathbb{A}$  is a phenomenological parameter modifying the gravitational waveform's dispersion relation. The  $\gamma$ -dependent distance measure  $D_\gamma$  (see Ref. [23] for exact formula) further depends on known astrophysical parameters (Hubble parameter, matter density parameter, etc.) of which we suppress errors on and take them as exact values for simplicity in the analysis [43]. Parameter  $\gamma$  governs the order of correction and  $\gamma = 0$  (PN-order 1.0) is what we're limited to since this is the only value contained in the ppE framework for the PN-order 3.5 `TaylorF2` model. Such MG-LV interpretations are generic models modifying the dispersion of a GW with more specific generation mechanism still yet to be explored. Ref. [14] notes some limitations in prescribing MG effects as modifications of the dispersion of the waveform. In LV-type modification further work in existing, model-independent approaches, e.g., the Standard Model Extension [44, 45], could be interesting (see for example Ref. [46]).

Constraints have been imposed on the wavelength of the graviton, the binary-pulsar constraint (serving as dynamical bounds) and solar-system constraints (serving as static bounds) provide the most reliable estimates [47]. Lorentz-violating parameter  $\mathbb{A}$  is unbounded in the grav-

itational sector. So, parameters are represented by,

$$\lambda_{\text{LV}} = 2\pi\text{\AA}^{-1/2}, \quad \lambda_g \geq \begin{cases} 1.6 \times 10^{10}[\text{km}], & \text{dynamic,} \\ 2.8 \times 10^{12}[\text{km}], & \text{static.} \end{cases}$$

For EDGB gravity, the constraint parameter is  $|\alpha_{\text{EDGB}}|$ . Here  $\zeta_3 = \xi_3 M^{-4} = 16\pi\alpha_{\text{EDGB}}^2 M^{-4}$ , with  $\beta \propto \zeta_3(1-4\eta)$ . In Brans-Dicke theory  $\beta \propto (s_{\text{BH,NS}} - s_{\text{BH,NS}})^2 \omega_{\text{BD}}^{-1}$ . From measurements of the Cassini spacecraft [48, 49] bounds on EDGB and Brans-Dicke parameters are,

$$|\alpha_{\text{EDGB}}|^{1/2} \leq 8.9 \times 10^6 \text{ km}, \\ \omega_{\text{BD}} > 4 \times 10^4.$$

With other suggested constraints [50, 51] giving,

$$|\alpha_{\text{EDGB}}|^{1/2} < 9.8 \text{ km}, \\ |\alpha_{\text{EDGB}}|^{1/2} < 7.1 \times 10^{-1} \text{ km}.$$

### C. Expansions

Similarly to Ref. [13] the additive noise to the GW signal is assumed to be stationary, statistically independent in each interferometer, and Gaussian with zero mean (non-Gaussian transients in the noise are expected to be vetoed by the detection algorithms), assuming statistical independence of the noise at different sites. The network probability distribution function (pdf) becomes the product of each pdf at separate interferometers.

We implement the analytic asymptotic expansion of the variance and bias developed in Refs. [11, 12] which is extended to a network of detectors in Ref. [13]. The general form for expansion of the variance and bias respectively follow as

$$\sigma_{\vartheta^i}^2 = \sigma_{\vartheta^i}^2[1] + \sigma_{\vartheta^i}^2[2] + \dots, \quad (2.2)$$

$$b_{\vartheta^i} = b_{\vartheta^i}[1] + b_{\vartheta^i}[2] + \dots, \quad (2.3)$$

with  $\sigma_{\vartheta^i}^2$  being the diagonal elements of the covariance matrix, where

$$\sigma_{\vartheta^i}[1], b_{\vartheta^i}[1] \propto \rho^{-1}, \\ \sigma_{\vartheta^i}[2], b_{\vartheta^i}[2] \propto \rho^{-2},$$

for network SNR  $\rho$ . This inverse proportionality continues at higher orders in similar fashion. Here the network SNR is the sum over the square of the optimal SNR  $\rho^I$  of the signal at the  $I$ -th detector,

$$\rho^2 = \sum_I (\rho^I)^2, \quad \rho^I = \langle s^I | s^I \rangle^{1/2} \quad (2.4)$$

Notice that  $\rho$  increases for a fixed source by increasing the number of detectors. Low-SNR regime present larger contributions of higher-order terms in the expansions, while high-SNR dependence allows first-order approximations in the expansion to be efficient in error analysis.

What is usually regarded as the error in a lab measurement is the square root of the mean-squared error (MSE),

where the MSE is the sum of the variance (2.2) and square of the bias (2.3):  $MSE_{\vartheta^i} = \sigma_{\vartheta^i}^2 + b_{\vartheta^i}^2$ . Since this analysis computes errors at second-order of  $1/\rho$ , the expression above only requires first-order of the bias which is negligible as already discussed in Ref. [13]. We estimate uncertainties of the two-dimensional ppE parameter space  $\theta_{\text{ppE}}^i$  for different  $\beta$  at a fixed exponential  $b$ . In addition, the inclusion of  $\theta_{\text{ppE}}^i$  to a signal's extrinsic and intrinsic parameter space  $\theta_{\text{phys}}^i$  is also assessed.

## III. RESULTS

In this section we explore the errors both as a function of the SNR and sky location of the source. To identify SNR dependencies and regions of lowest error estimates the sky dependencies of errors are observed through a 289-point sky grid. A point  $(\text{lat}_i, \text{long}_j)$  in latitude-longitude coordinates (of the Earth frame) on the sky grid follows from the procedure of Ref. [13] (detector coordinates also follow Ref. [13], which are fixed in the Earth Frame as given in Ref. [52, 53]).

As discussed in Section II,  $\epsilon = \pi/6$  is a fixed value and excluded in error analysis. Parameter  $\psi$  is also fixed and arbitrary values can be chosen for fiducial parameters  $\phi_c$  and  $t_c$ . The sky-averaged SNR is restricted to  $\rho < 20$  to focus on the more likely advanced interferometer scenarios. For each system considered, the distance of the resolved signal in the network is varied to keep a fixed SNR. For a three-detector network ( $I = H, L, V$ ) the following is chosen for the equal-mass binary systems:

- BBH 1:1-  $(m_1, m_2) = (10, 10)M_\odot$ ,  $D_L = 1100\text{Mpc}$ ,
- BNS-  $(m_1, m_2) = (1.4, 1.4)M_\odot$ ,  $D_L = 200\text{Mpc}$ .

Here the constructed BBH and BNS system leaves the network with an averaged SNR of  $\rho = 14.6$  and  $\rho = 17.0$ , respectively. For unequal mass systems we choose a BBH system with a 1:2 mass ratio and a BHNS binary with the following:

- BBH 1:2-  $(m_1, m_2) = (5, 10)M_\odot$ ,  $D_L = 850\text{Mpc}$ .
- BHNS-  $(m_1, m_2) = (1.4, 10)M_\odot$ ,  $D_L = 450\text{Mpc}$ .

which respectively give SNRs of  $\rho = 14.9$  and  $\rho = 15.8$ . For direction reconstruction and related extrinsic parameters the network geometry is important; however, for intrinsic parameters (as with the ppE parameters) SNR gains and losses have a larger impact [13].

Finally, errors in this section are indicated with,

$$\Delta\vartheta_i[1] = \sqrt{\sigma_{\vartheta^i}^2[1]}, \quad \Delta\vartheta_i[2] = \sqrt{\sigma_{\vartheta^i}^2[2]} \\ \Delta\vartheta_i[1+2] = \sqrt{\sigma_{\vartheta^i}^2[1] + \sigma_{\vartheta^i}^2[2]}. \quad (3.1)$$

For example first-order errors of the symmetric mass ratio  $\eta$  are marked by  $\Delta\eta[1]$ , second-orders are marked by  $\Delta\eta[2]$ , and total error with the inclusion of second-order contributions as  $\Delta\eta[1+2]$ .

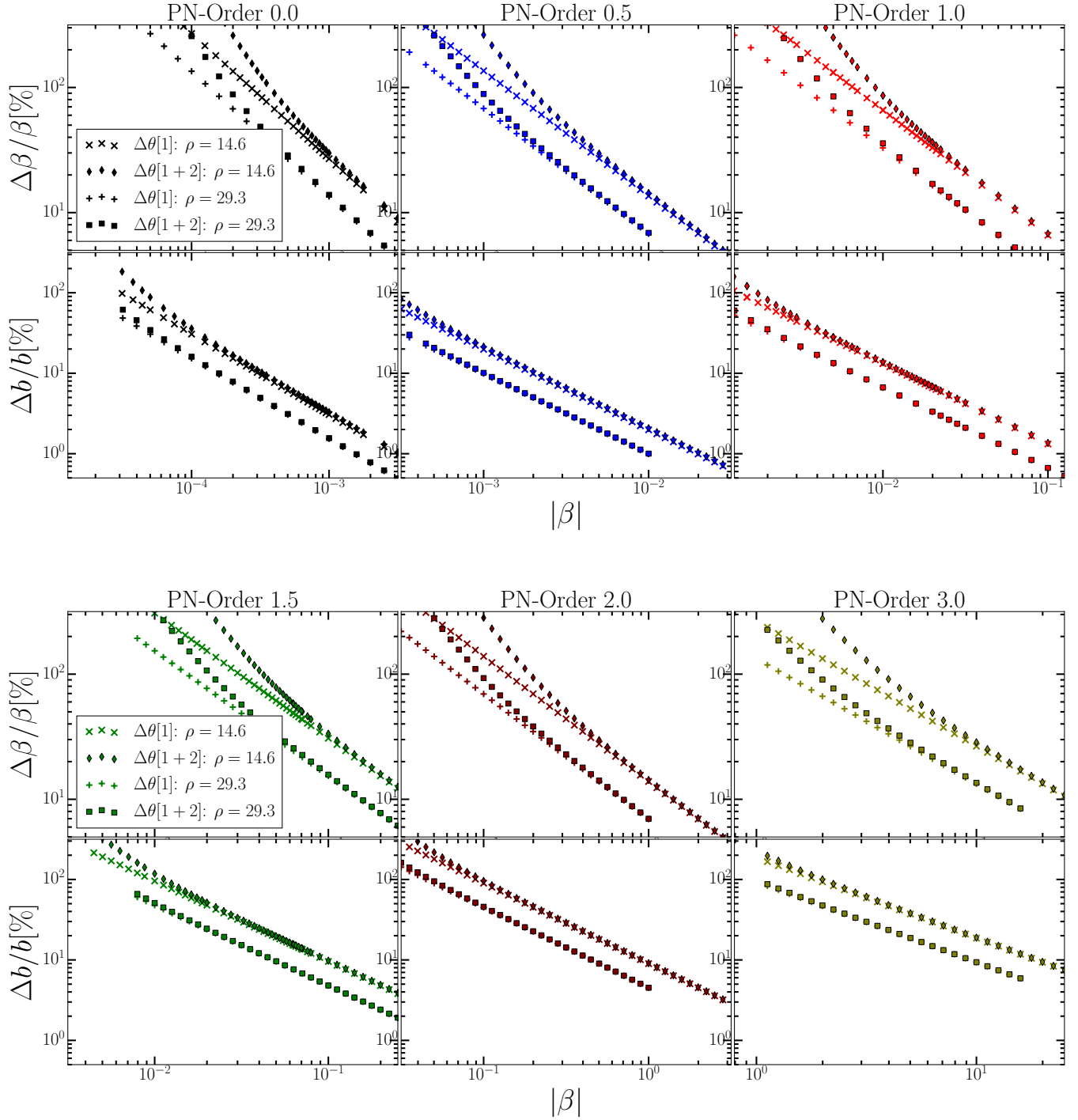


FIG. 2. Sky-averaged errors as a function of  $\beta$  for a two-dimensional ppE parameter space for the BBH 1:1 system of averaged network SNR  $\rho = 14.6$ . SNR results of  $\rho = 29.3$  are also shown by setting the distance to  $D_L = 550$  Mpc. As noted in Ref. [13] error estimates are rescaled as  $\sigma[1](\rho^*/\rho)$  and  $\sigma[2](\rho^*/\rho)^2$ , where  $\rho^*$  is the SNR that error estimates are originally calculated from. In the top panel the far left column represents each system for a PN-order 0.0 modification ( $b = -5$ ), the center column is a PN-order 0.5 modification ( $b = -4$ ), and far right column is for PN-order 1.0 modifications ( $b = -3$ ). Similarly, the bottom panel are resulting modifications at PN-order 1.5 ( $b = -2$ ), 2.0 ( $b = -1$ ), and 3.0 ( $b = +1$ ).  $\beta$  is more tightly constrained at lower PN-orders and the inclusion of second-order errors for  $(\beta, b)$  drastically diverge from Fisher estimates as  $\beta \rightarrow 0$ .

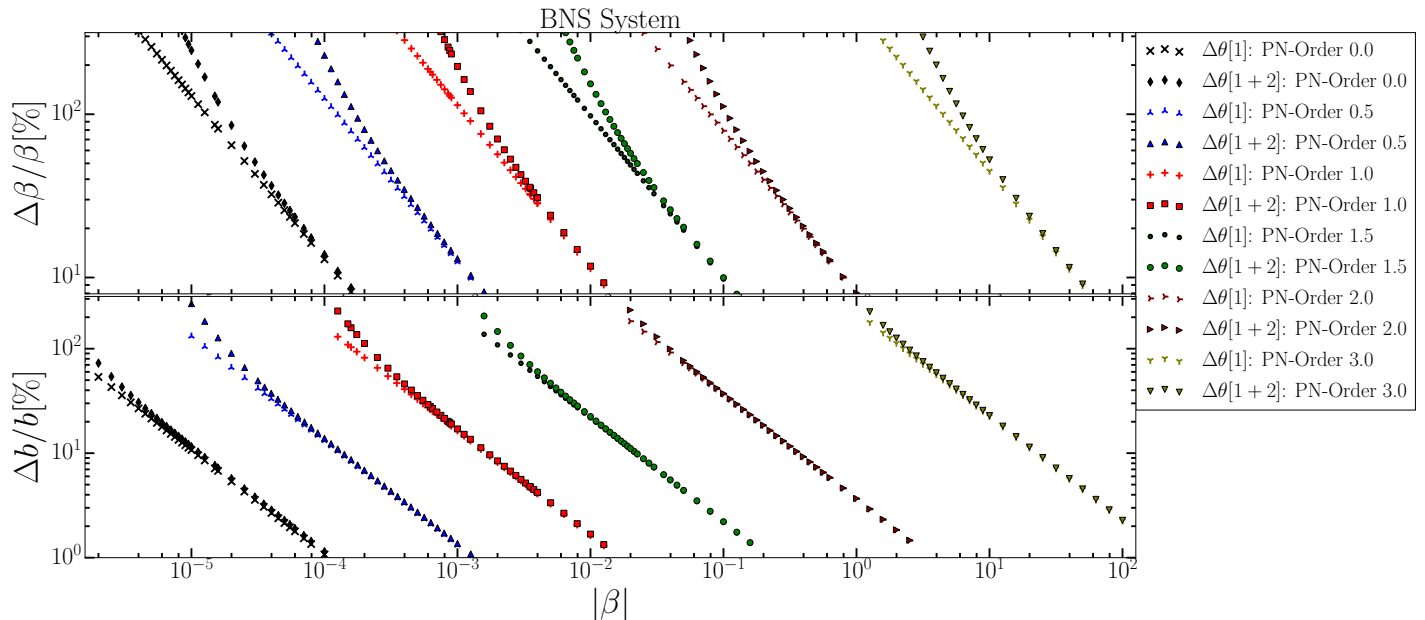


FIG. 3. Sky-averaged errors, similar to figure 2, for a BNS system of averaged SNR  $\rho = 17.0$ .

First-order Error (System)	PN-order 0.0	PN-order 0.5	PN-order 1.0	PN-order 1.5	PN-order 2.0	PN-order 3.0
$\Delta\beta[1]$ (BBH 1:1)	$2.70 \times 10^{-4}$	$1.36 \times 10^{-3}$	$6.59 \times 10^{-3}$	$3.07 \times 10^{-2}$	$1.39 \times 10^{-1}$	2.66
$\Delta\beta[1]$ (BNS)	$1.29 \times 10^{-5}$	$1.24 \times 10^{-4}$	$1.14 \times 10^{-3}$	$9.78 \times 10^{-3}$	$7.93 \times 10^{-2}$	4.49

TABLE I. Constant slopes of first-order error estimates of the BBH 1:1 (for SNR  $\rho = 14.6$ ) and BHNS systems for all  $\beta$  values. Here percent errors [%] follow a  $1/\beta$  relationship for  $\Delta\beta[1]$  represented above for respective PN-orders.

### A. Two-dimensional study: equal mass

In this subsection uncertainties for a two-dimensional parameter space are computed for both the BBH 1:1 and BNS systems, marked by  $\Delta\theta_{\text{ppE}}^i$ . Parameter  $b$  is chosen at a fixed PN-order correction with PN-order 0.0, 0.5, 1.0, 1.5, 2.0, and 3.0 (i.e.,  $b = -5, -3, -2, -1, +1$ ) while  $\beta$  is varied at each PN order. Here  $\beta$  probes values small enough to induce a sky-averaged error larger than 100% in  $b$  and large enough for  $\lesssim 10\%$  sky-averaged error in  $\beta$ . Errors for the BBH 1:1 system are depicted in figure 2, each labeled column representing a particular PN-order modification. Furthermore, to demonstrate the SNR dependence the BBH 1:1 system contains values for the scenario in which the SNR is doubled, for this the distance is decreased to  $D_L = 550$  Mpc. Figure 3 illustrates similar results for the BNS system.

The constant slopes of errors at first-order are catalogued in Table I for each PN-order. The computed first-order errors are consistent with statements of Ref. [16] which demonstrate that different PN-order corrections lead to different feasible constraints on  $\beta$ -values. BNS systems offer tighter constraints on  $\beta$  at each chosen  $b$ . Note however that scaling parameters controlling

propagating modifications, e.g. the graviton wavelength  $\beta_{\text{MG}} \propto \lambda_g^{-2}$ , are not more tightly constrained with BNS systems at shorter distances than BBH systems at larger distances. Rather, parameters like  $\beta_{\text{MG}}$ , also depend on a distance measure and masses of the compact objects that adversely affect constraints at shorter distances and smaller masses.

The smaller  $\beta$ , the more second-order effects in the errors contribute. As expected second-order effects on the errors of  $b$  are less significant, and errors  $> 100\%$  on  $\beta$  force sizeable second-order contributions in  $b$ . If  $b$  is near distinguishable,  $\Delta b[1+2] \lesssim 100\%$ ,  $\Delta\beta[1+2]$  are much larger than  $\Delta\beta[1]$ . Only when  $\Delta b[1+2] \lesssim 10\%$  do  $\Delta\beta[1]$  and  $\Delta\beta[1+2]$  become similar. Simulations producing the results of figures 2 and 3 used both  $\pm\beta$  values and the skewed representation of figure 1 is not apparent. Observing the range of  $\beta$  values, where the error is smaller than 100%, in figures 2 and 3, the constraints are significantly more stringent than previous studies [16].

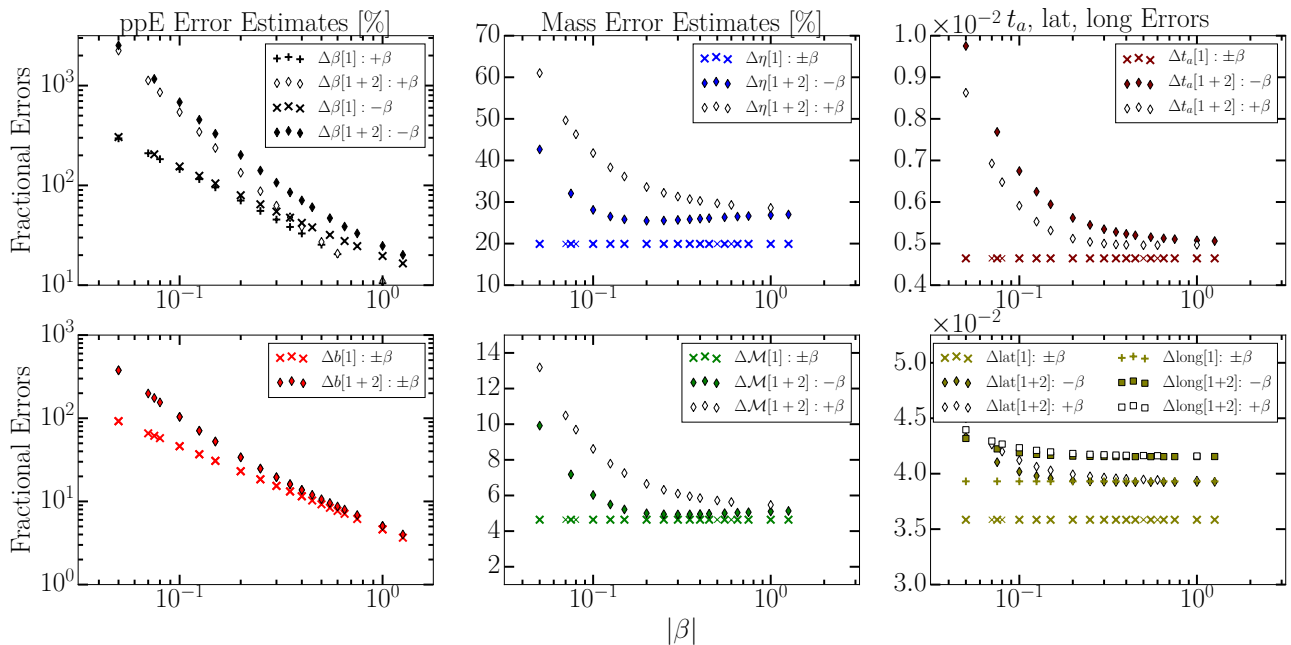


FIG. 4. Sky-averaged uncertainties for the equal-mass BBH 1:1 system for a PN-order 1.0 modification of the seven dimensional parameter space (ppE parameters  $\{\beta, b\}$  and physical parameters  $\{\eta, \log \mathcal{M}, t_c, \text{lat}, \text{long}\}$ ). In the left column the top panel displays  $\Delta\beta$  percent errors as a function of  $\beta$  (the sign of  $\beta$  provides different error estimates) and below that are  $\Delta b$  errors as a function of  $\beta$  (the sign of  $\beta$  does not play a role in these error estimates). In the middle and to the right are the physical parameters' errors, where the constraint of  $\beta$  primarily affects the second-order contributions. Enlarging the parameter space increases error estimates from those computed in figure 2 at PN-order 1.0, thus weakening constraints on  $\beta$ . For negative  $\beta$ , the full-dimensional study states  $\Delta\beta[1] = 100\%$  at  $\beta = -0.16$  and  $\Delta\beta[1+2] = 100\%$  at  $\beta = -0.32$ .

### B. Full parameter space: equal mass

In this subsection, first- and second-order uncertainties  $\Delta\vartheta^i$  of a full 7-dimensional parameter space are calculated for the equal-mass BBH 1:1 system, where  $\vartheta = \{\theta_{\text{ppE}}, \theta_{\text{phys}}\}$ . Here  $b$  is fixed to induce a PN-order 1.0 modification ( $b = -3$ ). Such corrections simulate effects produced by modifying the GW dispersion relation [6, 23]. Unlike the two-dimensional cases, the errors (first- and second-order) are effected by the sign of  $\beta$ , where sky-averaged errors for the ppE parameter pair ( $\beta, b$ ) are displayed in the left column of figure 4. Errors of physical parameters affected by varying  $\beta$  are depicted in the middle and right column of figure 4. The skewed behavior of  $\pm\beta$  results are representative of fitting factor results of figure 1.

For  $\beta$  the first-order errors are not at a constant slope.  $\Delta\beta[1]$  approximately follows linear relationship:  $\Delta\beta[1] \approx 0.046|\beta| + 0.15$ , for negative  $\beta$ . Here a 100% error occurs at  $\beta = -0.16$ , for  $\Delta\beta[1]$ , and  $\beta = -0.32$ , for  $\Delta\beta[1+2]$ . In this more realistic scenario, it can be seen that for extremely small  $\beta$  values  $b$  falls within its own uncertainty. Yet, analogous to the two parameter space, a 100% error in  $\Delta b[1+2]$  requires large errors in  $\Delta\beta[1+2]$ . Furthermore, error estimates are at least an order of magnitude larger. Another aspect of considering a

full-dimensional parameter space are the additional error trends imparted on physical parameters (masses, arrival time, etc) when  $\beta$  is varied, see the middle and right column of figure 4.

The sky distributions of the errors and the SNR are shown in figure 5. Table II catalogs this for  $-\beta = 0.25, 0.35, 0.55$ . This SNR dependence is similar to intrinsic parameters for GWs. The  $\beta$  values are chosen for the following reasons:

1. At  $\beta = -0.25$ , figure 4 identifies the conditions:  $\Delta b[2]/\Delta b[1] \approx 1$  with  $\Delta\beta[1] < 100\% < \Delta\beta[1+2]$ . Averages are performed before ratios. In  $\text{SNR} \gtrsim 15$ , we have  $\Delta b[2]/\Delta b[1] \lesssim 1$ , as seen in (a). (b) displays  $\Delta\beta[1+2]$ , which ranges from 66.4% to 468.7%.  $\Delta\beta[2]$  dominates the error budget. Error's extrema are displayed in Table II for future reference.
2. For  $\beta = -0.35$ , sky-averaged  $\Delta\beta[1] < \Delta\beta[1+2] \approx 100\%$ . Although  $\Delta b[2]/\Delta b[1] > 1$ , in limited portions of the sky, the ratio never exceeds 1.3 with a maximum of  $\Delta b[1+2] = 42.0\%$ . There is a strong increase in  $\Delta\beta[1+2]$  from  $\Delta\beta[1]$  in low SNRs. The majority of the sky is dominated by second-order terms, with  $\Delta\beta[2]/\Delta\beta[1]$  ranging from 0.91 to 2.72.

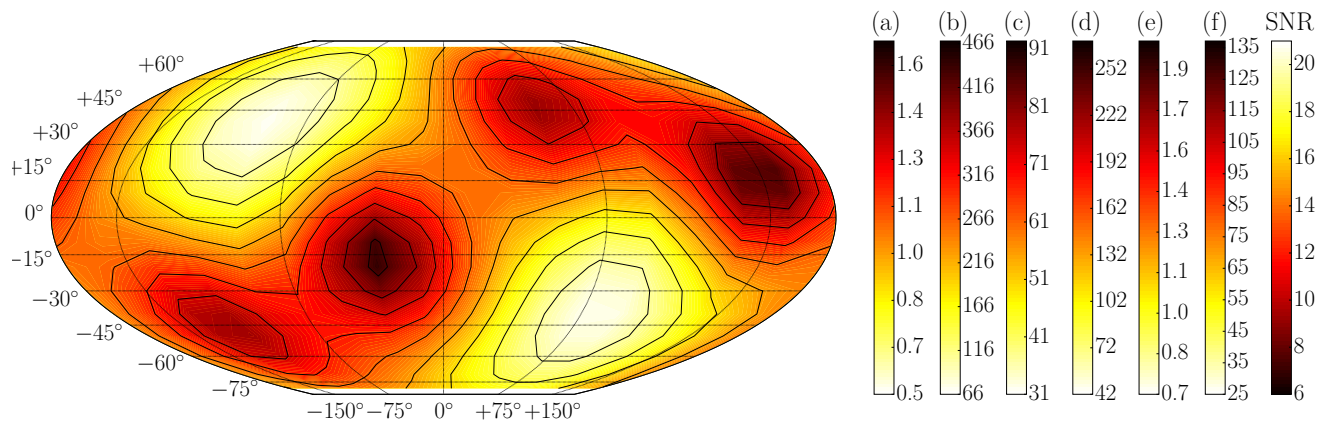


FIG. 5. Sky-map of error estimates, where color bars represent range of ppE quantities labeled (a), (b)..., (f) in Table II. This demonstrates the correlation of the SNR and ppE error estimation over the sky-grid. See text for discussion.

ppE $\beta$ -value	Error Estimations	$\rho_{\max} = 20.8$	$\rho_{\min} = 7.0$
-0.25			
(a)	$\Delta b[2]/\Delta b[1]$	0.55	1.67
	$\Delta b[1]$	12.1 [%]	36.2 [%]
	$\Delta b[1+2]$	13.8 [%]	70.5 [%]
	$\Delta\beta[2]/\Delta\beta[1]$	1.19	3.57
	$\Delta\beta[1]$	42.7 [%]	126.4 [%]
(b)	$\Delta\beta[1+2]$	66.4 [%]	468.7 [%]
-0.35			
	$\Delta b[2]/\Delta b[1]$	0.43	1.28
	$\Delta b[1]$	8.7 [%]	25.8 [%]
	$\Delta b[1+2]$	9.4 [%]	42.0 [%]
	$\Delta\beta[2]/\Delta\beta[1]$	0.91	2.72
(c)	$\Delta\beta[1]$	31.4 [%]	92.9 [%]
(d)	$\Delta\beta[1+2]$	42.4 [%]	269.1 [%]
-0.55			
	$\Delta b[2]/\Delta b[1]$	0.32	0.99
	$\Delta b[1]$	5.5 [%]	16.4 [%]
	$\Delta b[1+2]$	5.8 [%]	23.2 [%]
(e)	$\Delta\beta[2]/\Delta\beta[1]$	0.65	1.96
	$\Delta\beta[1]$	21.1 [%]	62.4 [%]
(f)	$\Delta\beta[1+2]$	25.2 [%]	137.3 [%]

TABLE II. Maxima and minima of estimates depicted in the sky-map plot (figure 5) for respective  $\beta$ -values of figure 4. Errors are the smallest for  $\rho_{\max} = 20.8$  and largest for  $\rho_{\min} = 7.0$ . Terms labeled with (a), (b)..., (f) correspond to respective color bars in figure 5. Values are chosen because they offer the most insight.

- $\beta = -0.55$  is where we calculate sky-averaged ratio  $\Delta\beta[2]/\Delta\beta[1] \approx 1$  with  $\Delta\beta[1] < \Delta\beta[1+2] < 100\%$ . Here larger portion of the sky has ratio  $\Delta\beta[2]/\Delta\beta[1] < 1$  as shown in (e). A majority (but not all) of the sky-map has total error falling be-

low 100% after the inclusion of second-orders with sky-averaged error at  $\Delta\beta[1+2] \approx 47\%$ .

From the known dependence on  $\rho$ , quantities displayed in figure 5 and Table II can be derived for higher or lower SNRs.

### C. Full parameter space: unequal mass

Here first- and second-order uncertainties  $\Delta\vartheta^i$  of a full seven-dimensional parameter space are calculated for the BBH 1:2 and BHNS system. In this construct a weak-field  $b = -7$  modification is induced, which in our context mimics the non-spinning, even-parity sector of quadratic modified gravity (QMG) and can include specifics like EDGB gravity. Inclusion of QMG modifications is due to  $\beta$  being resolvable by a non-zero mass differences at this PN-order. These modifications manifest through modification of the energy flux as  $\beta \propto \zeta_3(1 - 4\eta)$  [34] and the BHNS binary can also test examples of dipole gravitational radiation, like Brans-Dicke (BD).

Error estimations results are presented in figure 6. The overall trend of this system's estimates are similar to the results of the equal-mass BBH 1:1 of the previous subsection, with a few exceptions. The first being that the separation between errors  $\Delta\beta[1], \Delta b[1]$  and  $\Delta\beta[1+2], \Delta b[1+2]$  are not as great as with the PN-order 1.0 modification. In comparison to the previous subsection, the chirp mass errors  $\Delta\mathcal{M}$  are roughly the same, yet  $\Delta\eta$  estimates are considerably less. Time of arrival errors  $\Delta t_a$  are also less and latitude-longitudinal estimates don't suffer from varying  $\beta$  at first- and second-order.

For the BBH 1:2 system sky contours of mass and ppE error estimates at, respectively,  $|\beta| = 1.8 \times 10^{-4}$  and  $|\beta| = 3.0 \times 10^{-4}$  are displayed in figures 7 and 8. In figure 7, the mass error estimates are plotted since this  $\beta$ -value produces sky-averaged estimate  $\Delta\beta[1+2] < 100\%$ , with second-order effects in the mass estimates making

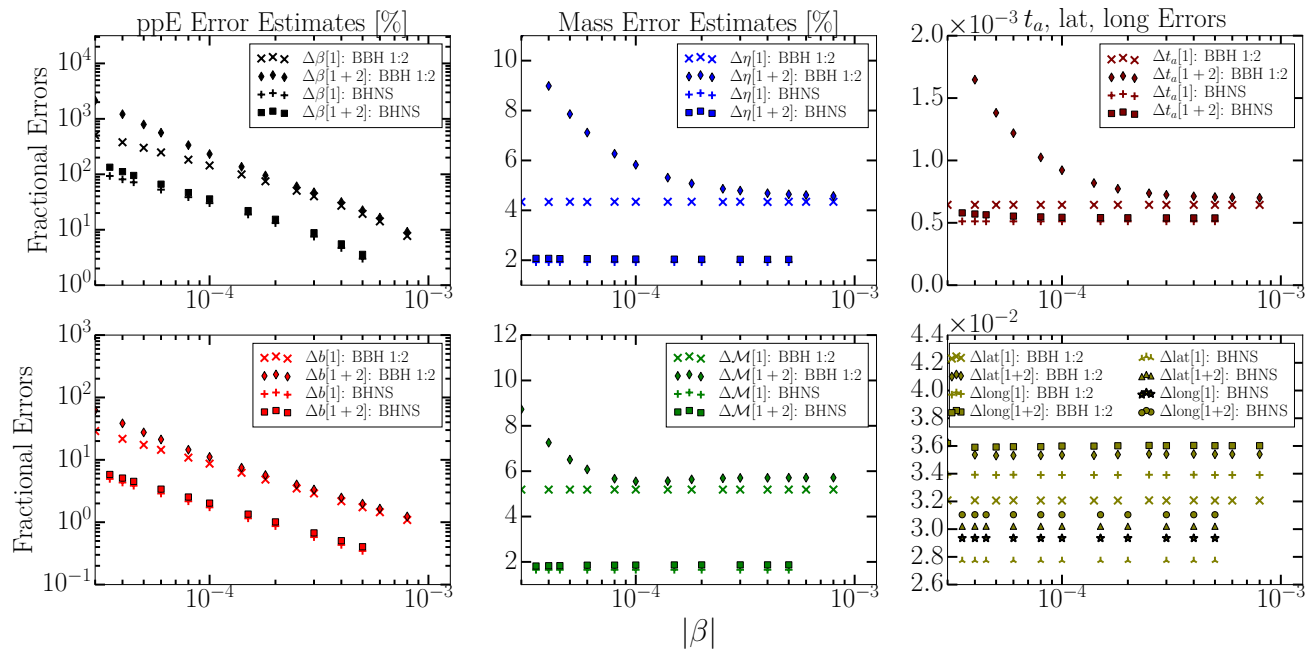


FIG. 6. This figure depicts sky-averaged error estimates for the BBH 1:2 and BHNS system. The left column represent calculations of the ppE parameter errors ( $\Delta\beta, \Delta b$ ) for negative  $\beta$ -values, center column are the mass errors ( $\Delta\eta, \Delta\mathcal{M}$ ), and far right are arrival time  $\Delta t_a$  and latitude-longitude ( $\Delta\text{lat}, \Delta\text{long}$ ) error estimates. Results are restricted to negative  $\beta$ . Here latitude-longitude error estimates are not effected by  $\beta$  variation, as was previously presented in the equal-mass system. This study states that  $\Delta\beta_{\text{BBH1:2}[1+2]} = 95.2\%$  at  $\beta_{\text{BBH1:2}} = -1.8 \times 10^{-4}$  and  $\Delta\beta_{\text{BHNS}[1+2]} = 95.3\%$  at  $\beta_{\text{BHNS}} = -4.5 \times 10^{-5}$ .

notable contributions (see figure 6). We observe that in such a context second-order effects do not dominate the error budget of  $\Delta\eta$  and  $\Delta\mathcal{M}$  in this sky-grid. In low-SNR regions  $\Delta\eta[2]/\Delta\eta[1]$  and  $\Delta\mathcal{M}[2]/\Delta\mathcal{M}[1]$  ratios are near unity. In these same low-SNR regimes  $\Delta\beta[2]/\Delta\beta[1] > 1$  and  $\Delta\beta[1+2] > 100\%$ , which demonstrates the sky-grid SNR relation to errors accrued on physical parameters due to large error estimates of ppE parameters.

Figure 8 represents a similar sky-map, but here contours are generated for  $|\beta| = 1.8 \times 10^{-4}$  modifications and color bars are representative of ppE parameter error estimates ( $\Delta\beta, \Delta b$ ). Contours are plotted at this  $\beta$ -value since this simulates the condition that  $\Delta\beta[1+2] \approx 100\%$  with  $\Delta\beta[1] < 100\%$ . Again we observe the volatility in  $\Delta\beta[1+2]$  estimates, ranging from 53% to about 250% while remaining strongly correlated to the SNR. One notable feature of this plot is that ratios  $\Delta b[2]/\Delta b[1]$  and  $\Delta\beta[2]/\Delta\beta[1]$  are relatively close to each other, being approximately equal to each other in regions of high-SNR. This is in contrast to the equal-mass study of the previous subsection and demonstrates the small separation in  $\Delta\beta[1]$  and  $\Delta\beta[1+2]$  estimates depicted in the left column of figure 6, which allows the ratio  $\Delta b[2]/\Delta b[1]$  to be comparable to  $\Delta\beta[2]/\Delta\beta[1]$ . Relations between these quantities depicted in figure 7 and 8 can be compared to the maxima and minima of the equal-mass BBH system of PN-order 1.0 modifications catalogued in Table II. Similar results come from the BHNS system.

In order to check that the Fisher information matrix did not become singular we systematically explored its eigenvalues. For example figure 9 shows scenarios in which the Fisher matrix becomes singular for the seven dimensional study. These values of  $\beta$  were avoided in this analysis.

#### D. Application to explicit alternative theories

Since the modification considered in subsection III B occur at PN-order 1.0 in the phase, an analysis can be done from these results for the massive graviton model. Progression of sky-averaged errors for  $\Delta\beta[1+2]$ , calculated from negative  $\beta$ -values, of figure 4 imposes a constraint of  $|\beta_{\text{MG}}| \leq 0.31$ . Existing constraints are  $|\beta_{\text{MG, static}}| \leq 0.37$ , based on current static bounds on  $\lambda_g$  (see section II B) computed from the BBH 1:1 system at 1100 Mpc. This asymptotic approach thus produces an additional 16.2% constraint on existing bounds at  $1\sigma$ . When including second-order terms in error estimation the constraints on  $\lambda_g$  have a fractional increase of 30% from the first-order Fisher matrix approach. Given these results, further constraints on the graviton wavelength  $\lambda_g$  may be possible, even with second-order error terms accounted for. From calculated results the sky-averaged

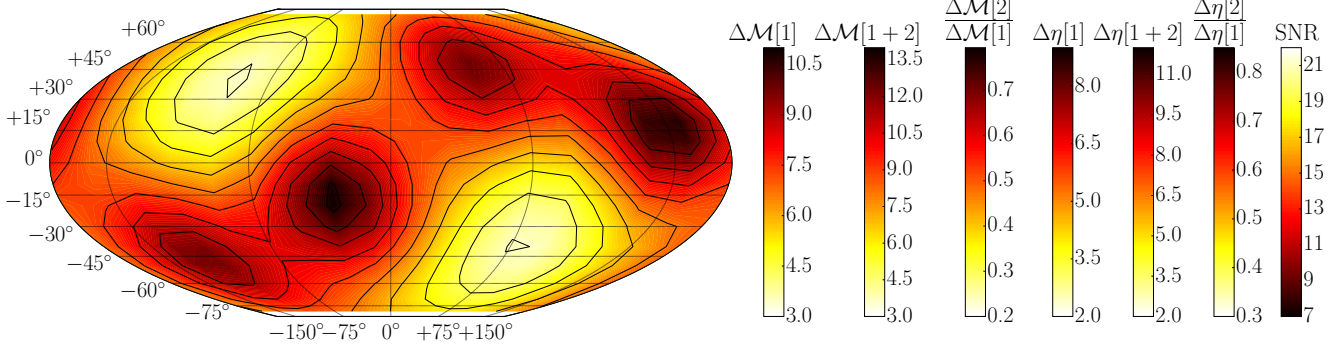


FIG. 7. Sky-map error estimates of mass parameters  $\Delta\eta$  and  $\Delta\mathcal{M}$  simulated at  $\beta_{\text{BBH1:2}} = -3.0 \times 10^{-4}$  of figure 6. Here mass errors, intrinsic to the binary system, also vary in proportion to SNR. Sky-average estimates provide  $\Delta\beta_{\text{BBH1:2}}[1+2] = 47.4\%$ .

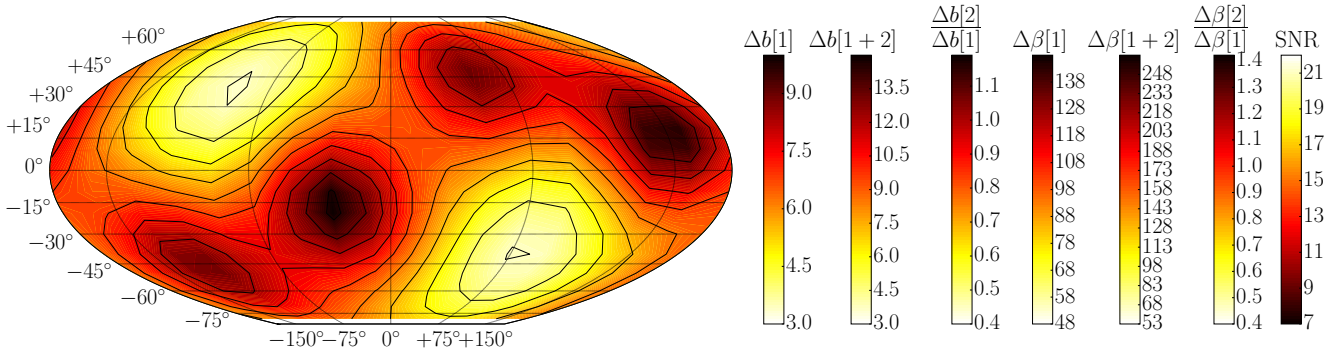


FIG. 8. Sky-map error estimates of ppE parameters  $\Delta\beta$  and  $\Delta b$  simulated at  $\beta_{\text{BBH1:2}} = -1.8 \times 10^{-4}$  of figure 6. Sky-average estimates provide  $\Delta\beta_{\text{BBH1:2}}[1+2] = 95.2\%$ .

feasible bounds are displayed in Table III.<sup>2</sup>

Distinguishability constraint ( $\lesssim 100\%$ Error)	
$\lambda_{g,\text{LV}} > 3.04 \times 10^{12}$ km	(BBH 1:1)
$\xi_3^{1/4} < 7.17$ km	(BBH 1:2)
$ \alpha_{\text{EDGB}} ^{1/2} < 2.69$ km	(BBH 1:2)
$\xi_3^{1/4} < 1.34$ km	(BHNS)
$ \alpha_{\text{EDGB}} ^{1/2} < 5.02 \times 10^{-1}$ km	(BHNS)
$\omega_{\text{BD}} > 12.7(s_{\text{NS}} - 0.5)^2$	(BHNS)

TABLE III. Seven-dimensional study of the BBH 1:1, 1:2, and BHNS systems with feasible constraints, i.e., computed MSE  $\lesssim 100\%$ . The first considers PN-order 1.0 modifications and the latter two consider  $b = -7$  modifications. Included are the graviton wavelength (or generic Lorentz-violating) dispersion modification and non spinning, even-parity sector models of QMG (EDGB parameter included). Brans-Dicke constraint depends on sensitivity parameter  $0.2 \leq s_{\text{NS}} \leq 0.3$ .

Bayesian assessments in the ppE framework of unequal mass systems (of 1:2 and 1:3 ratios) with SNR of 20 put constraints at  $\lambda_g > 8.8 \times 10^{12}$  km [16]. Other Bayesian studies also conclude that advanced detectors would generally not favor a MG theory over that of GR when  $\lambda_g$  is larger than the most stringent static bounds [17]. In this respect, our errors impart a more conservative approach to error estimation that still suggest that constraints may still be improved. In this case the Bayesian studies impose tighter constraints.

An application of seven-dimensional results presented in subsection III C for the BBH 1:2 can also be made. This  $b = -7$  modification has  $\beta_{\text{QMG}} \propto \xi_3(1 - 4\eta)$ . In this context the constraint parameter is  $\zeta_3 = \xi_3 M^{-4}$  in the non-spinning, even-parity sector of QMG, where  $\xi_3 = 16\pi\alpha_{\text{EDGB}}^2$  in EDGB gravity [34]. For the BBH 1:2 system figure 6 presents  $\Delta\beta[1] = 99.7\%$  at  $|\beta| = 1.4 \times 10^{-4}$  and  $\Delta\beta[1+2] = 95.2\%$  at  $|\beta| = 1.8 \times 10^{-4}$ . These computations translate to respective inputs in Table III for  $\xi_3$  and  $\alpha_{\text{EDGB}}$ . Strongest suggested constraints have

<sup>2</sup> This is at the same order of projected bounds on  $\lambda_g$  determined from previous Fisher analysis for BBH systems of  $m_1 = m_2 =$

$10M_\odot$  with similar SNR values, though each make use of different source parameters and detectors [20, 22].

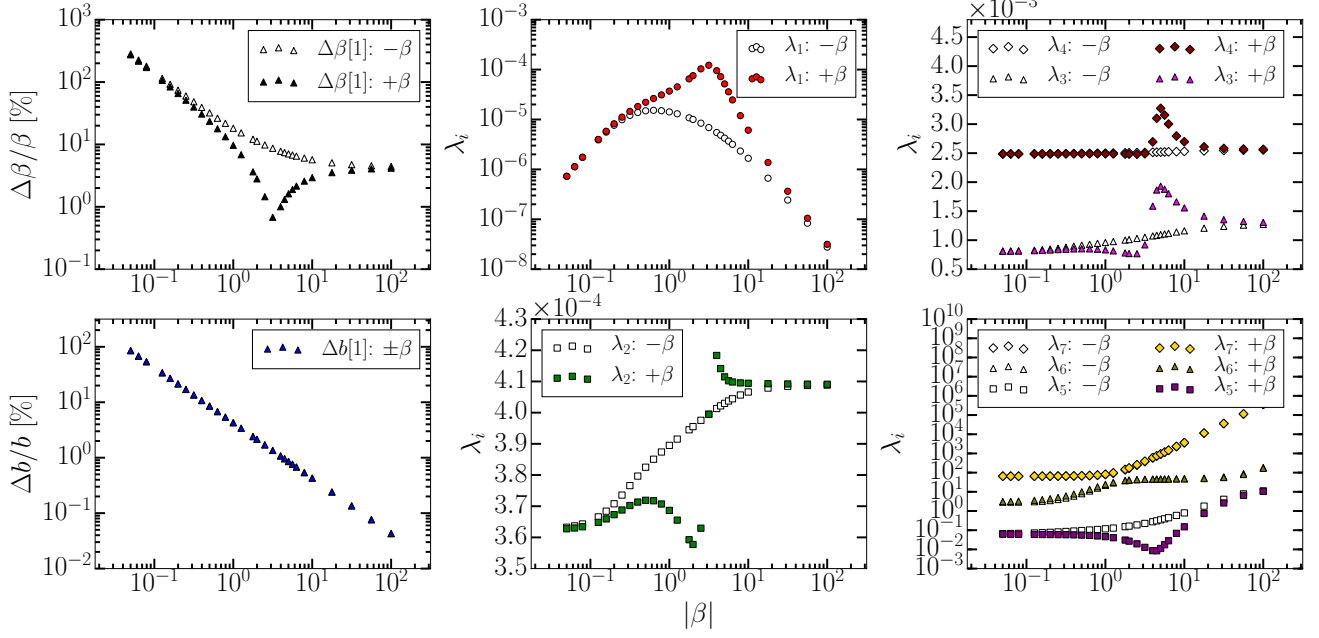
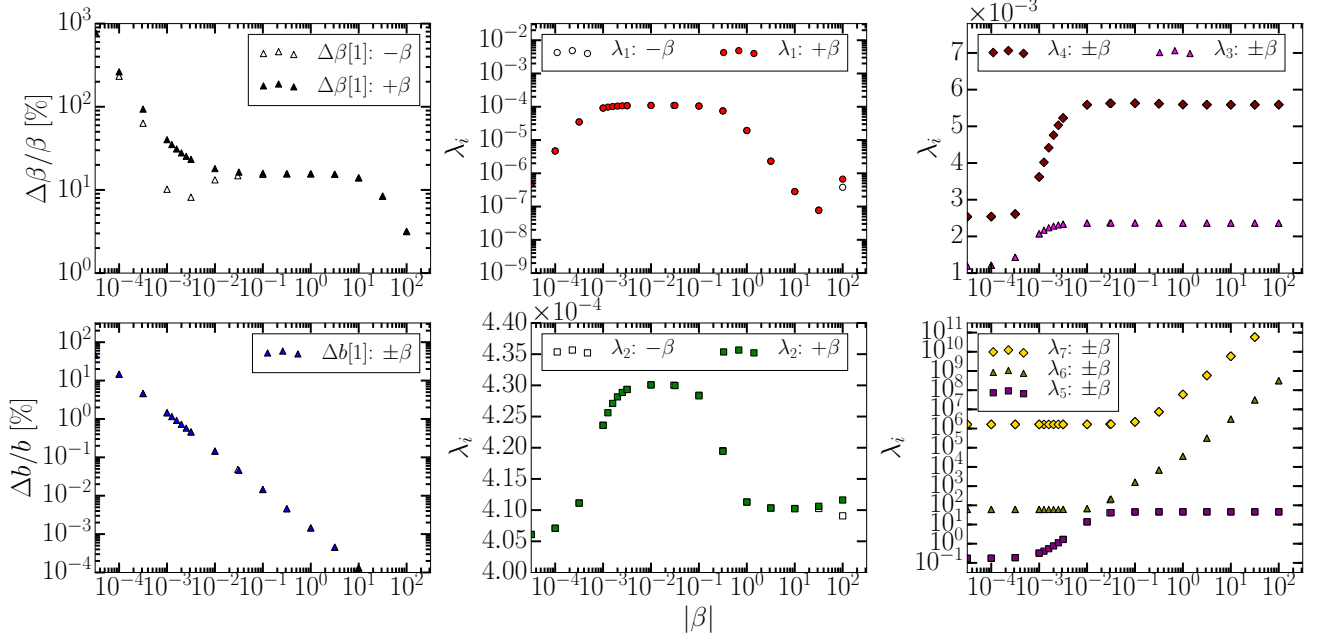
Seven-dimensional ppE Errors and Parameter Space Eigenvalues:  $b = -3$ Seven-dimensional ppE Errors and Parameter Space Eigenvalues:  $b = -7$ 

FIG. 9. First order errors (left panels) and eigenvalues (center and right panels) of the Fisher matrix when computations are extended to the seven dimensional parameter space.

quoted  $\xi_3^{1/4} < 26$  km and  $\xi_3^{1/4} < 1.9$  km, or in terms of EDGB gravity  $|\alpha_{\text{EDGB}}|^{1/2} < 9.8$  km and  $|\alpha_{\text{EDGB}}|^{1/2} < 0.71$  km [50, 51]. In weak-field tests the Cassini spacecraft has provided  $|\alpha_{\text{EDGB}}|^{1/2} < 8.9 \times 10^6$  km (i.e.,  $\xi_3^{1/4} < 2.4 \times 10^7$  km) [48]. Bayesian results estimate  $\xi_3^{1/4} \lesssim 11$  km (or  $|\alpha_{\text{EDGB}}|^{1/2} \lesssim 4$  km) at an SNR of 20 [34] which is

quoted in Ref. [6] as  $\xi_3^{1/4} \lesssim 20$  km for an SNR of 10.

Similar application to QMG and EDGB theories can be done with results of the BHNS system. These constraints are also presented in Table III and are more stringent than the BBH 1:2 system. With BHNS systems Brans-Dicke can be investigated through  $\beta_{\text{BD}} \propto (s_1 - s_2)^2 \omega_{\text{BD}}^{-1}$ , where constraint parameter is  $\omega_{\text{BD}}$  with  $s_{\text{BH}} = 0.5$  for

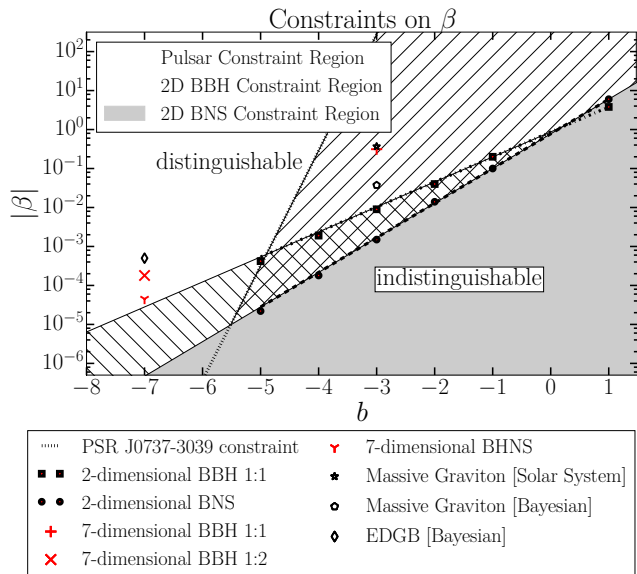


FIG. 10. Constraints on ppE parameters  $(\beta, b)$ . Alongside frequentist mean-squared error  $\lesssim 100\%$  estimates are constraints imposed by Bayesian estimates [16], solar system tests [47], and binary pulsar measurements [36, 37]. Regions below each mark/line are where violations cannot be detected based on each respective study. The GR-limit is  $\beta = 0$ . Our frequentist two-dimensional study considers ppE parameter space  $(\beta, b)$ , while seven-dimensional studies includes physical parameters (masses, etc.). See text for discussion.

black holes and for neutron stars  $0.2 \leq s_{\text{NS}} \leq 0.3$  [39–42]. Figure 6 results indicate  $\Delta\beta[1] = 95.3\%$  at  $|\beta| = 4.5 \times 10^{-5}$  for the BHNS system. Thus, constraints results in  $\omega_{\text{BD}} \geq 1.14$  and  $\omega_{\text{BD}} \geq 0.51$  at  $s_{\text{NS}} = 0.2$  and  $s_{\text{NS}} = 0.3$ , respectively. Results of the Cassini spacecraft have also established  $\omega_{\text{BD}} > 4 \times 10^4$  [49]. In Ref. [19] Fisher estimates placed constants of  $\omega_{\text{BD}} > 194$  for a BHNS systems of similar masses.

#### IV. CONCLUSION

Figure 10 provides a summary of the main results of this paper. The mean-squared error (MSE) estimates from compact binaries studied is shown, each mark represents the lower boundary of the  $(\beta, b)$ -parameter space where the MSEs are larger than 100% and therefore not resolvable. Previous Bayesian studies correspond to the range of exponential ppE parameter:  $-11 \leq b \leq 2$ . The fact that for the massive graviton case ( $b = -3$ ) our approach here, which is a more realistic lower limit of the Crame Rao lower bound, rules out results that were allowed by a Bayesian study, seems to indicate the need of a careful evaluation of the role of the priors.

Results of the higher order asymptotic analysis of the frequentist approach to error estimation states that fur-

ther constraints can be imposed on existing non-GR theories with the study of the seven-dimensional parameter space (see Table III). This approach does not involve the use of priors and improves upon the CRLB estimator for low-SNR detections. Here the graviton wavelength can be constrained by an additional 16.2% as compared to current static bounds [47]. Yet, these projected constraints do not extend Bayesian estimates of the graviton wavelength. Further studies present the scenario for the weak-field  $b = -7$  modification, which can include quadratic modified gravity (QMG) (specifics being EDGB gravity) and Brans-Dicke type modifications (figure 6). For the non-spinning, even-parity sector of QMG, bounds suggest further constraints are possible as compared to current bounds placed by Bayesian estimates and Cassini constraints. Furthermore, error estimates for modifications at both PN-order 1.0 and the  $b = -7$  weak-field follow similar sky-map contours, which are correlated to the SNR patterns (see figures 5 and 8).

General results show that for successively higher PN-order modifications, set by  $b$ , the separation between first- and second-order errors increase (see figures 2 and 3). Such an effect percolates to the seven-dimensional study. Errors also increase as the parameter space is enlarged, where the two-dimensional studies provide overly optimistic errors. As constraints on  $\beta$  become tighter in the seven-dimensional studies, the effects of second-order estimates also accrue on physical parameters, namely  $\eta$ ,  $\mathcal{M}$ ,  $t_a$ , and latitude-longitude parameters (see figures 4 and 6). Finally, SNR increases translate error estimates as discussed in Ref. [13] (figure 2), so all results can be rescaled as a function of the SNR.

Calculations performed in this paper are for single detection scenarios. With multiple detections the presence of weak, but consistent, violations could be combined to make a stronger statement about error estimations. Such methods to *resolve* consistent signals were explored in a Bayesian framework in Ref. [14] and it is left for future studies in the frequentist framework. Furthermore, as waveform models advance, for both the inspiral and ppE framework, the application of our MLE asymptotic expansion could be applied to spinning binaries or to waveforms that include the merger and ringdown phases. This will add insight into additional modified theories mappable into the ppE framework.

#### V. ACKNOWLEDGEMENTS

The authors would like to thank S. Vitale, T.G.F. Li, A.J. Weinstein, and W.D. Pozzo for useful discussion and comments. R. Tso is supported by the National Science Foundation Graduate Research Fellowship Program under Grant No. DGE-1144469, the Ford Foundation Pre-doctoral Fellowship, and the Gates Graduate Fellowship.

## Appendix A: Notation and network signal

Masses of each compact body are labeled as  $m_{1,2}$ , the total mass being  $M = m_1 + m_2$  with  $\nu = (\pi M f)^{1/3}$  and  $\eta = m_1 m_2 / M^2$  as the reduced mass frequency and symmetric mass ratio, respectively. The usual chirp mass is  $\mathcal{M} = \eta^{3/5} M$ . Geometrized units ( $G = c = 1$ ) are also employed [54]. Terms labeled with  $I$  indicate a particular quantity for that  $I$ -th detector, e.g.,  $s^I$  is a signal received at some  $I$ -th detector,  $\rho^I$  is a detector-dependent SNR, etc. Finally, the detectors considered are those for Adv. LIGO and Adv. Virgo, so we have  $I = H, L, V$  for the respective advanced interferometers in Hanford USA, Livingston USA, and Cascina Italy. Quantities summed over  $I$  indicate the total network contribution of that term, e.g., network SNR, network Fisher matrix. Apart from units employed notation follows that of Ref. [35].

To discuss some of the terms appearing in (1.1):  $\tau_I$  is a time lag parameter accounting for the delay in the waveform's propagation from the  $I$ -th detector frame (IDF) to some fiducial frame (FF),<sup>3</sup> with  $\mu^I$  and  $\Phi_0^I$  being coefficients that depend on the inclination angle  $\epsilon$  of the binary system and the generalized antenna patterns  $\mathcal{F}_{+,x}^I$  of each detector. These are represented by,

$$\tau_I = \hat{\mathbf{n}} \cdot (\mathbf{r}_I - \mathbf{r}_{FF}), \quad (\text{A1})$$

$$\mu^I = \left( \left( \frac{1}{2} \mathcal{F}_+^I (1 + \cos^2 \epsilon) \right)^2 + (\mathcal{F}_x^I \cos \epsilon)^2 \right)^{1/2}, \quad (\text{A2})$$

$$\Phi_0^I = \arctan \frac{2\mathcal{F}_x^I \cos \epsilon}{\mathcal{F}_+^I (1 + \cos^2 \epsilon)}, \quad (\text{A3})$$

with  $\hat{\mathbf{n}}$  the direction of travel of the waveform,  $\mathbf{r}_I$  the distance to the  $I$ -th detector (i.e., the IDF origin), and  $\mathbf{r}_{FF}$  the distance to the FF origin. Reasons for construction of a frame of common origin is due to the feasibility and efficiency displayed in calculations of quantities in particular frames. Notion of a common origin between the frames is valid since approximative measures<sup>4</sup> allow the origins of the coordinate systems to coincide. With respect to Ref. [13] the frames are established as the already mentioned IDF and FF, with a third frame called the wave-frame (WF).<sup>5</sup> In producing calculable quantities the frames are then fixed to values of that in the Earth frame (EF).

Since the origins of the frames coincide transformation between the frames is feasible through simple Eulerian angles with the usual ZXZ convention [55]. From this, a set of Euler angles  $(\phi, \theta, \psi)$  converts a quantity from the FF into the WF and another set  $(\alpha^I, \beta^I, \gamma^I)$  converts

from the FF into the IDF through the usual rotation matrices. Here angle  $\psi$  is the polarization angle. A variety of relations can be uncovered after defining a few new angles. Let angle pairs  $(\Phi, \Theta)$  and (long, lat) describe the sources location in the sky (the former being in spherical coordinates and the latter in longitude-latitude coordinates), let  $(\Xi, \zeta)$  be defined from projections of  $\hat{\mathbf{n}}$  onto the FF's axis, define angles  $(\Omega^I, \Upsilon^I)$  so that they prescribe the location of the  $I$ -th detector with respect to the FF, and allow angle  $\Delta^I$  to span the region between the first detector arm (in the IDF) and the local northern direction. These relations are summarized as follows:

$$\phi = \Phi - \frac{\pi}{2} = \text{long} - \frac{\pi}{2} = \Xi + \frac{\pi}{2} \quad (\text{A4})$$

$$\theta = \pi - \Theta = \frac{\pi}{2} + \text{lat} = \zeta$$

and

$$\alpha^I = \Omega^I + \frac{\pi}{2}, \quad \beta^I = \frac{\pi}{2} - \Upsilon^I, \quad \gamma^I = \Delta^I + \frac{\pi}{2}. \quad (\text{A5})$$

Formulation of  $\mathcal{F}_{+,x}^I$  into a symmetric-trace-free base has been performed, with respect to the Eulerian angle dependence, and what surfaces in the frequency represented signal are the two generalized antenna patterns:

$$\mathcal{F}_+^I = \frac{1}{2} \left( T_{2s}(\alpha^I, \beta^I, \gamma^I) + T_{-2s}(\alpha^I, \beta^I, \gamma^I) \right) \quad (\text{A6})$$

$$\times \left( T_{2s}^*(\phi, \theta, \psi) + T_{-2s}^*(\phi, \theta, \psi) \right)$$

$$\mathcal{F}_x^I = \frac{i}{2} \left( T_{2s}(\alpha^I, \beta^I, \gamma^I) - T_{-2s}(\alpha^I, \beta^I, \gamma^I) \right) \quad (\text{A7})$$

$$\times \left( T_{2s}^*(\phi, \theta, \psi) - T_{-2s}^*(\phi, \theta, \psi) \right)$$

where  $T_{mn}$  are second-order Gel'fand functions ( $T_{mn}^*$  being their complex conjugates). Function statements, such as  $f(\alpha^I, \beta^I, \gamma^I)$  and  $g(\phi, \theta, \psi)$ , represent their dependencies on Euler angle rotations from  $FF \rightarrow IDF$  and  $FF \rightarrow WF$ , respectively. See Ref. [13] for exemplary calculations. Note that an auxiliary ppE template has been developed that considers extra polarizations of waveforms produced in non-GR gravity, incorporating additional propagating degrees of freedom in the ppE framework [29]. Although it is of interest to measure extra polarizations expected in a variety of alternative theories of gravity, these extra modes lead to more complex models. For initial analysis of modified gravity through the asymptotic MLE approach a ppE template, with only the standard two propagating modes, is considered both sufficient and satisfactory for now. Ref. [56] investigated methods to test non-GR polarizations via continuous waveforms from asymmetric pulsars.

<sup>3</sup> FF is the frame in which the origins are referenced to coincide.

<sup>4</sup> Through reasonable assumption of zero curvature over the course of the GW's propagation and introduction of time lag  $\tau_I$ .

<sup>5</sup> Determined through the GW's direction of travel and orthonormal WF unit vectors along its axis, where dominant harmonic polarizations in the waveform is assumed

- 
- [1] G.M. Hardy (for the LIGO Scientific Collaboration), *Classical Quantum Gravity* **27**, 084006 (2010).
- [2] <https://www.advancedligo.mit.edu>
- [3] <https://wwwcascina.virgo.infn.it/advirgo>
- [4] C.M. Will, *Living Rev. Relativity* **9**, 3 (2006).
- [5] J.R. Gair, M. Vallisneri, S.L. Larson, J.G. Baker, *Living Rev. Relativity* **16**, 7 (2013).
- [6] N. Yunes, X. Siemens, *Living Rev. Relativity* **16**, 9 (2013).
- [7] N. Yunes, F. Pretorius, *Phys. Rev. D* **80**, 122003 (2009).
- [8] K.G. Arun, B.R. Iyer, M.S.S. Qusailah, B.S. Sathyaprakash, *Classical Quantum Gravity* **23**, L37-L43 (2006).
- [9] C.K. Mishra, B.R. Iyer, M.S.S. Qusailah, B.S. Sathyaprakash, *Phys. Rev. D* **82**, 024006 (2006).
- [10] C.K. Mishra, K.G. Arun, B.R. Iyer, B.S. Sathyaprakash, *Phys. Rev. D* **82**, 064010 (2010).
- [11] S. Vitale, Z. Zanolin, *Phys. Rev. D* **82**, 124065 (2010).
- [12] M. Zanolin, S. Vitale, N. Makris, *Phys. Rev. D* **81**, 124048 (2010).
- [13] S. Vitale, M. Zanolin, *Phys. Rev. D* **84**, 104020 (2011).
- [14] T.G.F. Li, W.D. Pozzo, S. Vitale, C.V.D. Broeck, M. Agathos, J. Veitch, K. Grover, T. Sidery, R. Sturani, A. Vecchio, *Phys. Rev. D* **83**, 082003 (2012).
- [15] T.G.F. Li, W.D. Pozzo, S. Vitale, C.V.D. Broeck, M. Agathos, J. Veitch, K. Grover, T. Sidery, R. Sturani, A. Vecchio, *J. Phys.: Conf. Ser.* **363**, 012028 (2012).
- [16] N. Cornish, L. Sampson, N. Yunes, F. Pretorius, *Phys. Rev. D* **84**, 062003 (2011).
- [17] W.D. Pozzo, J. Veitch, A. Vecchio, *Phys. Rev. D* **83**, 082002 (2011).
- [18] D.S. Sivia, J. Skilling, in *Data Analysis: A Bayesian Tutorial, 2nd ed.* (Oxford University Press, New York, 2006).
- [19] C.M. Will, *Phys. Rev. D* **50**, 6058-6067 (1994).
- [20] C.M. Will, *Phys. Rev. D* **57**, 2061 (1998).
- [21] A. Pai, K.G. Arun, *Classical Quantum Gravity* **26**, 155002 (2009)
- [22] D. Keppel, P. Ajith, *Phys. Rev. D* **82**, 122001 (2010).
- [23] S. Mirshekari, N. Yunes, C. Will, *Phys. Rev. D* **85**, 024041 (2012).
- [24] A. Buonanno, B.R. Iyer, E. Ochsner, Y. Pan, B.S. Sathyaprakash, *Phys. Rev. D* **80**, 084043 (2009).
- [25] K.G. Arun, B.R. Iyer, B.S. Sathyaprakash, Pranesh A. Sundararajan, *Phys. Rev. D* **71**, 084008; *Phys. Rev. D* **72**, 069903 (E) (2005).
- [26] T.A. Apostolatos, *Phys. Rev. D* **52**, 605 (1995).
- [27] B.S. Sathyaprakash, S.V. Dhurandhar, *Phys. Rev. D* **44**, 3819 (1991).
- [28] C.M. Bender, S.A. Orszag, in *Advanced Mathematical Methods for Scientists and Engineers I, Asymptotic Methods and Perturbation Theory* (Springer, New York, 1999).
- [29] K. Chatziioannou, N. Yunes, N. Cornish, *Phys. Rev. D* **86**, 022004 (2012).
- [30] M. Vallisneri, N. Yunes, *Phys. Rev. D* **87**, 102002 (2013).
- [31] *Advanced LIGO anticipated sensitivity curves*, LIGO Document T0900288-v3
- [32] F. Acernese, et al. (VIRGO), *Classical Quantum Gravity* **32**, 024001 (2015).
- [33] N. Yunes, L.C Stein, *Phys. Rev. D* **85**, 104002 (2011).
- [34] K. Yagi, L.C Stein, N. Yunes, T. Tanaka, *Phys. Rev. D* **85**, 064022 (2012).
- [35] M. Maggiore, in *Gravitational Waves* (Oxford University Press, New York, 2007, Vol. 1).
- [36] N. Yunes, S.A. Hughes, *Phys. Rev. D* **82**, 082002 (2010).
- [37] A.G Lyne, et al, *Science* **303**, 1153 (2004).
- [38] K. Yagi, N. Yunes, T. Tanaka, *Phys. Rev. Lett.* **109**, 251105 (2012).
- [39] J. Healy, T. Bode, R. Haas, E. Pazos, P. Laguna, D.M. Shoemaker, N. Yunes, *Classical Quantum Gravity* **29**, 232002 (2012).
- [40] S. Mirshekari, C.M. Will, *Phys. Rev. D* **87**, 084070 (2013)
- [41] N. Yunes, P. Pani, V. Cardoso, *Phys. Rev. D* **85**, 102003 (2012)
- [42] H.W. Zaglauer, *Astrophys. J.* **393**, 685-696 (1992)
- [43] J. Beringer, et al. (Particle Data Group), *Phys. Rev. D* **86**, 010001 (2012).
- [44] V.A. Kostelecký, D. Colladay, *Phys. Rev. D* **58**, 116002 (1998)
- [45] V.A. Kostelecký, *Phys. Rev. D* **69**, 105009 (2004).
- [46] V.A. Kostelecký, J.D. Tasson, *Phys. Lett. B* **749**, 551 (2015).
- [47] E. Berti, J. Gair, A. Sesana, *Phys. Rev. D* **84**, 101501 (2011).
- [48] L. Amendola, C. Charmousis, S.C. Davis, *J. Cosmol. Astropart. Phys.* **10**, 004 (2007).
- [49] B. Bertotti, L. Iess, P. Tortora, *Nature* **425**, 374-376 (2003).
- [50] P. Pani, E. Berti, V. Cardoso, J. Read, *Phys. Rev. D* **84**, 104035 (2011)
- [51] K. Yagi, *Classical Quantum Gravity* **29**, 075005 (2012)
- [52] B. Allen, arXiv:9607075 (1996).
- [53] B.F. Schutz, *Classical Quantum Gravity* **25**, 125023 (2011).
- [54] C.W. Misner, K.S. Thorne, J.A. Wheeler, in *Gravitation* (W.H. Freeman, San Francisco, 1973).
- [55] H. Goldstein, in *Classical Mechanics* (Addison-Wesley, Reading, MA, 1980, 2nd Ed.).
- [56] M. Isi, A.J. Weinstein, C. Mead, M. Pitkin, *Phys. Rev. D* **91**, 082002 (2015)